# The Impact of Aluminum and Iron Substitution on the Structure and Electrochemistry of $Li[Ni_{0.4}Co_{0.2-y}M_yMn_{0.4}]O_2$ Materials

James D. Wilcox[a], Efrain E. Rodriguez[b], and Marca M. Doeff[a]

a) Materials Sciences Division

Lawrence Berkeley National Laboratory

University of California

Berkeley, CA 94720

and

b) Lujan Neutron Scattering Center

Los Alamos National Laboratory

Los Alamos, NM 87545

**Abstract**

$Li[Ni_{0.4}Co_{0.2-y}M_yMn_{0.4}]O_2$ ($0 \leq y \leq 0.2$) (M=Al) and $Li[Ni_{0.4}Co_{0.15}Fe_{0.05}Mn_{0.4}]O_2$ compounds were prepared in order to investigate the effect of replacement of all or part of the cobalt on the structural and electrochemical properties. The impact of substitution on the structure has been examined by both x-ray and neutron diffraction experiments. The incorporation of aluminum has minimal effect on the anti-site defect concentration, but leads to structural changes that affect electrochemical performance. The most important effect is an opening of the lithium slab dimension upon substitution, which results in improved rate performance compared to the parent compound. In contrast, the lithium slab dimension is not affected by iron substitution and no rate enhancement effect is observed. The cycling stability of aluminum containing materials is superior to both the parent material and iron-substituted materials.

**Introduction**

$LiCoO_2$ has been a mainstay of commercial lithium ion batteries since their introduction by Sony in 1991.[1] However, concerns over the high cost, toxicity, and the limited abuse tolerance of $LiCoO_2$ has led to a prolonged effort to find replacement cathode materials for the next generation of lithium ion batteries. Mixed transition metal oxides of composition $Li[Ni_yCo_{1-2y}Mn_y]O_2$ have been extensively studied for the purpose of designing cathode materials with optimal capacity, rate capability, and thermal/structural stability.[2] In particular, the compositions $Li[Ni_{1/3}Co_{1/3}Mn_{1/3}]O_2$ and $Li[Ni_{0.4}Co_{0.2}Mn_{0.4}]O_2$ have been widely characterized and are capable of delivering in

excess of 160 mAh/g when cycled to 4.2-4.4 V and over 200 mAh/g to potentials above 4.6-4.7 V.[3, 4, 5, 6]

The current-carrying capability of an intercalation electrode material operating under standard cycling conditions is largely determined by the rate at which lithium ions can be transported through the host lattice. Using *ab initio* calculations, the activation energy for lithium ion diffusivity in the lamellar α-$NaFeO_2$ (space group $R\bar{3}m$) structure has been shown to be highly sensitive to the dimension of the lithium layer.[7, 8, 9] To maximize the lithium slab spacing and create high rate materials it is critical to minimize the number of anti-site defects where a transition metal, typically nickel, is found to reside on the *3a* site in the lithium plane.[10] Due to its small ionic radius compared to lithium (0.76 Å), cobalt in the low spin state (0.545 Å) minimizes the anti-site defect concentration in both $Li[Ni_{1-y}Co_y]O_2$ and $Li[Ni_{0.4}Co_{0.2}Mn_{0.4}]O_2$ systems and stabilizes the layered structure.[11, 12, 13, 14] Another strategy is to synthesize the structurally analogous sodium-containing phase, which contains very few antisite defects, and then ion exchange it to form the lithiated analog.[15]

Aluminum, which has an ionic radius of 0.535 Å, may be expected to have a similar effect on structure as cobalt.[16] Recent work on the $Li[Ni_{1/3}Co_{1/3-y}Al_yMn_{1/3}]O_2$ system shows that aluminum can be substituted up to y=0.25 without the formation of a γ-$LiAlO_2$ impurity phase.[17] This leads to higher *c/3a* ratios (a measure of lamellarity) and a general improvement in rate capability, when powders are prepared as in reference 17. Aluminum substitution into layered oxides has also been shown to have a positive effect on the thermal abuse tolerances of layered oxides, either by inhibiting

lithium extraction at high states of charge, or by chemical stabilization of the structure itself.[18, 19, 20]

$LiFeO_2$ does not crystallize in the layered α-$NaFeO_2$ structure, but either as tetragonally distorted γ-$LiFeO_2$ or the cubic α-$LiFeO_2$.[21, 22, 23, 24] Both the γ-$LiFeO_2$ and α-$LiFeO_2$ structure lack a long range diffusion pathway for lithium and the associated electrochemistry activity is limited.[25, 26] Single phase $Li[Ni_{1-x}Fe_x]O_2$ and $Li[Ni_{1/3}Co_{1/6}Fe_{1/6}Mn_{1/3}]O_2$ materials with the α-$NaFeO_2$ structure have been prepared although the electrochemical performance is generally observed to suffer from decreased capacity and increased capacity fade upon substitution.[17, 27, 28] This effect has been correlated with a strong increase in anti-site defect concentration at elevated iron contents leading to poor lithium ion transport and an increased difficulty in oxidizing nickel in the presence of iron.[29, 30]

In this work, we discuss the impact of aluminum and iron substitution on the structure and electrochemistry of $Li[Ni_{0.4}Co_{0.2-y}M_yMn_{0.4}]O_2$ and its implications for the design of low cobalt content metal oxides.

**Experimental**

All materials were synthesized using the glycine nitrate combustion method as described in references 17 and 31.

Powder X-ray diffraction (XRD) was performed in the range of 10°-70° 2Θ on a Phillips X'Pert diffractometer with an X'celerator detector using Cu Kα radiation. A custom milled polycarbonate powder holder was used to avoid any peak overlap associated with the holder material.[17] Neutron diffraction studies were undertaken on the Neutron Powder Diffractometer (NPDF) at the Lujan Neutron Scattering Center at

Los Alamos National Laboratory. Neutron powder diffraction was used in addition to powder XRD since it is sensitive to both light and heavy atoms and therefore affords more accurate information on the structural parameters. In addition, NPDF is a high-resolution, time-of-flight diffractometer that can probe high ranges in Q (or low d-spacings). Samples ranging in size from 1-2 g were sealed in vanadium sample holders and data was collected for 6-12 hours under ambient conditions. Unit cell parameters and site occupancy factors were obtained from a combined XRD/neutron diffraction Rietveld refinement using the General Structure Analysis System (GSAS/EXPGUI) software package.[32, 33]

Particle morphology studies were conducted using a field emission-scanning electron microscope (FESEM, Jeol JSM-6340F) and transmission electron microscope (TEM) (Phillips CM200FEG (field emission gun)) at an accelerating voltage of 200 kV. To prepare samples for TEM, powders were ground in a mortar and pestle in acetone and transferred to a holey carbon grid. Elemental analysis was done by inductively coupled plasma optical emission spectrometry (ICP-OES) (Columbia Analytical Services, Tucson, AZ).

Pressed pellets for conductivity studies were fabricated by uni-axially pressing ~0.5 g of active material to 5 kpsi in a ½" stainless steel die. The pellets were transferred into balloon holders and cold isostatically pressed to 180 kpsi achieving a green density of ~70% of the theoretical density calculated from diffraction data. To achieve further densification, pellets were packed in a getter material of the same composition and fired to 800° C for 48 hours in air. The pellet faces were polished flat and parallel and a final density of close to 75% was obtained. Thin gold electrodes

were sputtered on to each face of the pellet using a Bal-Tec SCD 050 sputter coater. AC impedance spectra were obtained using a Solartron Instruments 1260 impedance/gain-phase analyzer at selected temperatures between 25 and 200° C. Conductivities were derived from the intercept of the capacitative arc with the Z' axis in the Nyquist plots.

Laminate composite cathodes comprised of 84 wt.% active material, 8 wt.% poly(vinylidine fluoride) (PVDF, Kureha Chemical Ind. Co. Ltd.), 4 wt.% compressed acetylene black, and 4 wt.% SFG-6 synthetic flake graphite (Timcal Ltd., Graphites and Technologies) were prepared by applying slurries in 1-methyl-2-pyrrolidinone onto carbon coated current collectors (Intelicoat Technologies) by automated doctor blade. After drying in air and in vacuum for at least 24 hours, 1.8 $cm^2$ electrodes having an average loading of 7-10 $mg/cm^2$ of active material were punched out. Coin cells (2032) were assembled in a helium filled glove box with lithium metal anodes and 1M $LiPF_6$ in 1:2 ethylene carbonate/dimethyl carbonate (EC/DMC) electrolyte solution (Ferro). Galvanostatic cycling was carried out on an Arbin BT/HSP-2043 cycler between limits of 2.0 and 4.3-4.7V. All cells were charged at a current density of 0.1 $mA/cm^2$ independent of the discharge rate. Galvanostatic intermittent titration technique (GITT) experiments were conducted on a Macpile II (Bio-Logic, S.A., Claix, France) potentiostat/galvanostat between rest potentials of 2.0 and 4.4 V. Current pulses of 0.135 mA lasting 40.5 minutes were used on both charge and discharge corresponding to approximately 3-4% of the total cell capacity being passed on each titration step. The cell was equilibrated for four hours after each pulse prior to taking the next step.

## Results and Discussion

*$Li[Ni_{0.4}Co_{0.2-y}Al_yMn_{0.4}]O_2$ ($0 \leq y \leq 0.2$)*

All of the compounds were determined to be phase-pure by XRD and could be indexed to the $R\bar{3}m$ space group over the entire substitution range ($0 \leq y \leq 0.2$) (Figure 1). Powders ranged in color from a black/gray at y=0 to slightly red at higher aluminum contents. TEM images of the parent material, $Li[Ni_{0.4}Co_{0.2}Mn_{0.4}]O_2$, and the completely aluminum-substituted material, $Li[Ni_{0.4}Al_{0.2}Mn_{0.4}]O_2$, are presented in Figure 2a and b. The powders consist of small primary particles with an average diameter of approximately 50 nm, agreeing well with the particle size determined during Rietveld refinement (35-50 nm). The level of substitution had no discernible impact on particle morphologies. Primary particles are agglomerated into secondary particles that vary in diameter from approximately 250-500 nm. A typical SEM image is shown in Figure 2c.

Elemental analysis by ICP-OES indicated that the true compositions are very close to nominal ones, although there is a slight excess of lithium (2-8%) in samples with $y \leq 0.1$.

The results of a Rietveld analysis on the combined X-ray and neutron diffraction experiments on $Li[Ni_{0.4}Co_{0.2}Mn_{0.4}]O_2$ are shown in Figure 3. Table 1 contains structural parameters derived from these analyses on all of the compounds. The *a* unit cell parameter shifts inversely with y, contracting 0.1% in the fully Al-substituted material. The *c* unit cell parameter increases 0.03Å (0.2%) over the same range. The ionic radius of $Al^{3+}$ (0.535 Å) is somewhat smaller than that of low spin $Co^{3+}$ (0.545 Å)[14] causing a small decrease in the *a* unit cell parameter. The Li-O bond is lengthened, causing the observed expansion of the lithium slab dimension (*I*) and the *c* unit cell parameter. The

anti-site defect concentration, measured by the amount of nickel residing on the *3a* position ($Ni_{3a}$), is lowest in the aluminum free material but increases less than 1% upon the substitution of aluminum and is statistically unchanged in the range $0.05 \leq y \leq 0.2$.

Pressed pellet conductivities of $Li[Ni_{0.4}Co_{0.2-y}Al_yMn_{0.4}]O_2$ materials were obtained as a function of temperature using AC impedance measurements. These two-probe experiments do not allow ionic and electronic contributions to the conductivity to be distinguished, although the latter typically dominates in layered metal oxides of this type, in contrast to the situation with olivines.[34] It is clear from the data shown in the Arrhenius plot in Figure 4 that increasing Al substitution reduces overall conductivity in this series. $Li[Ni_{0.4}Co_{0.2}Mn_{0.4}]O_2$ has the highest conductivity ($1.1 \times 10^{-5}$ S/cm at 75° C), but it is still several orders of magnitude lower than that of $LiCoO_2$ ($10^{-3}$ S/cm at room temperature).[35] Aluminum substitution at even low levels reduces it even further; e.g. to $1.2 \times 10^{-6}$ S/cm for y=0.05 and to $2.2 \times 10^{-8}$ S/cm for y=0.1. This is consistent with the substitution of an *sp*-type metal for cobalt in these systems.[36] Aluminum has no available *d*-states near the Fermi energy and therefore, cannot participate in electron transport process during cycling. DOS calculations on similar materials confirm this, showing a decrease in the number of occupied states near the Fermi level as Al content increases.[37] These observations imply that it is reasonable to assume that electronic conductivity is indeed adversely affected by Al substitution.

Activation energies calculated from the Arrhenius plots are presented in Table 2, and increase as a function of y. The magnitude of these values is also consistent with an activated, small polaron conduction mechanism.[12]

Aluminum is an electrochemically inactive element under normal cycling conditions; thus the theoretical capacity shifts inversely with y in $Li[Ni_{0.4}Co_{0.2-y}Al_yMn_{0.4}]O_2$. It decreases from 279 mAh/g in the parent material (y=0) to 239 mAh/g upon full replacement of Co with Al (y=0.2). Additionally, X-ray absorption spectroscopy experiments,[38,39] first principle calculations,[40, 41] and iodometric titration results on chemically de-lithiated layered oxides[42] suggest that $Co^{3+}$ is not electroactive below about 4.3 V vs. $Li/Li^+$.[43] This suggests that practical capacities under normal cycling conditions may be unaffected as long as no other properties are grossly affected by aluminum substitution.

The discharge capacities of $Li/Li[Ni_{0.4}Co_{0.2-y}Al_yMn_{0.4}]O_2$ ($0 \leq y \leq 0.2$) coin cells cycled between 2.0 and 4.3 V vs. $Li/Li^+$ are presented in Figure 5a. The un-substituted material delivers 163 mAh/g on the first discharge cycle but fades nearly 6% in the first twenty cycles. Initial discharge capacities decrease in proportion to the Al content but cycling losses are reduced to 2-3% over 20 cycles for all but the y=0.2 cathode material. Thus, the performance of the y=0.05 compound matches or exceeds that of the unsubstituted analog after just a few cycles although the initial discharge capacity is slightly lower (159 mAh/g).

Aluminum substitution raises the potential at which lithium is extracted and re-inserted from the host lattice. This is most obvious when comparing differential capacity (dQ/dV) plots of materials galvanostatically cycled to 4.3V (Figure 6). The broad peaks are consistent with a topotactically occurring single-phase reaction and their shapes are relatively unchanged upon aluminum substitution. The peak charge potential shifts from 3.795 V when y=0 to a maximum of 3.958 V when y=0.2,

however. Likewise, upon cell discharge, the peak potentials increase from 3.747 V at y=0 to 3.903 V at y=0.2. This phenomenon has been predicted by *ab initio* calculations[36] and has been observed in other aluminum-substituted oxide materials.[43 44] The increased cell potential reduces the amount of lithium that can be removed upon charge to 4.3 V and results in lower discharge capacities upon the subsequent discharge.

Raising the charge cutoff potential to 4.7 V (Figure 5b) results in improved utilization for all the electrodes, although it comes at the expense of accelerated capacity fading. The effect is most pronounced for $Li[Ni_{0.4}Co_{0.2}Mn_{0.4}]O_2$, which gives 204 mAh/g or 73% of theoretical between 4.7 and 2.0V. In contrast, the capacity of $Li[Ni_{0.4}Al_{0.2}Mn_{0.4}]O_2$ only increases to 149 mAh/g or 62% of the theoretical. However, cells containing Al-substituted compounds exhibit better capacity retention than those with $Li[Ni_{0.4}Co_{0.2}Mn_{0.4}]O_2$.

Figure 7a-e shows first cycles of $Li/LiNi_{0.4}Co_{0.2-y}Al_yMn_{0.4}O_2$ ($0 \leq y \leq 0.2$) cells charged and discharged at 0.1 $mA/cm^2$ between 4.3 or 4.7 and 2.0V. For cells containing the Al-substituted materials charged to 4.7V, there is a sharp upswing in the cell potential near the end of charge. The somewhat premature polarization reflects the difficulty of removing lithium completely from structures containing aluminum, preventing complete utilization even when the charge cutoff potential is increased.

Lithium transition metal oxide cathode materials are known to suffer from poor coulombic efficiencies during the initial charge/discharge cycle. Such first cycle irreversible capacity losses have been attributed to structural changes in the layered metal oxides[39] and/or irreversible oxidation of electrolyte.[45] The table included in Figure 7 shows average values of the irreversible capacity losses obtained for each type

of cell in this study. When the charge was limited to 4.3V, an increase in this value was observed for cathode materials containing Al. The irreversible capacity losses increased substantially for all cells when the potential limit was raised to 4.7, although the magnitude of the increase was relatively lower for Al-substituted materials.

Discharge profiles of Li/Li[$Ni_{0.4}Co_{0.2-y}Al_yMn_{0.4}$]$O_2$ ($0 \leq y \leq 0.2$) cells at various current densities are presented in Figures 8a-e, and a modified Peukert plot is shown in Figure 8f, summarizing the results. The performance of Li[$Ni_{0.4}Co_{0.2}Mn_{0.4}$]$O_2$ is clearly very sensitive to the current density. In contrast, utilization is better at higher rates for cells with Al-containing cathode materials. In particular, it is noteworthy that higher capacities are achieved above 0.5 mA/$cm^2$ for Li[$Ni_{0.4}Co_{0.15}Al_{0.05}Mn_{0.4}$]$O_2$ than for Li[$Ni_{0.4}Co_{0.2}Mn_{0.4}$]$O_2$. A similar rate enhancement effect has been observed for partially Al-substituted compounds in the Li[$Ni_{1/3}Co_{1/3-y}Al_yMn_{1/3}$]$O_2$ series.[17] This was attributed to increases in the *c/3a* ratios, a structural parameter correlated to the degree of lamellarity. A decrease in anti-site mixing results in higher *c/3a* ratios; however, Al-substitution in the Li[$Ni_{0.4}Co_{0.2-y}Al_yMn_{0.4}$]$O_2$ ($0 \leq y \leq 0.2$) system has little effect on the amount of Ni on *3a* sites (Table 1). In spite of this, the lithium slab dimension (*I (*$LiO_2$*)*) becomes larger with higher Al content due to the structural effects of substitution. . The activation energy for lithium diffusion has been shown to be highly sensitive to this value.[7, 15] Expansion of the lithium slab diminishes the magnitude of the steric compression of the lithium ion in the activated state as well as the lithium-transition metal electrostatic interaction. Thus, reducing anti-site mixing below a certain level may not be necessary for improved electrochemical performance, if the lithium slab spacing can be increased by other means, as is apparently the case here. This

structural effect in the Al-substituted compounds is reflected in the decreased polarization observed in the discharge curves at the higher current densities in Figure 8a-e.

GITT experiments[46] were carried out on Li/Li[$Ni_{0.4}Co_{0.2-y}Al_yMn_{0.4}$]$O_2$ ($0 \le y \le 0.2$) cells between rest potentials of 2.0 and 4.4V versus $Li/Li^+$. Although absolute values of diffusion coefficients cannot be obtained because of limitations associated with the use of porous electrodes in these experiments, it should be possible to compare relative values as a function of state-of-charge and to compare the behaviors of the positive electrode materials, which all have similar physical properties. With these caveats in mind, relative Li diffusion coefficients as a function of state-of-charge during cell charge were calculated, and are presented in Figure 9. These values are presented as dimensionless ratios with respect to the initial diffusion coefficient measured for $Li_x[Ni_{0.4}Co_{0.2}Mn_{0.4}]O_2$ at x=1 ($D_{Li}/D^{\circ}_{Li,\,y=0}$). At the beginning of the charging process $D_{Li}$ is nearly the same for all materials independent of y, even though the overall conductivities were observed to vary by nearly four orders of magnitude. During the initial stages of lithium extraction the chemical diffusion coefficients decrease, reaching minima near x=0.8, possibly reflecting a weak charge ordering effect[47, 48] Alternatively, these variations can be explained by a decrease in the thermodynamic factor as the lithium content is reduced below x=1.[49] $D_{Li}$ then increases somewhat due to an expansion of the lithium slab dimension and an increase in lithium di-vacancy concentration, and finally decreases dramatically near the end of charge. (This does not necessarily coincide with complete lithium removal, particularly for materials with high Al content). Al substitution has the most pronounced effect on $D_{Li}$ at lower lithium

contents, and has very little effect at the beginning of charge, particularly for compounds where y≤0.1.

Due to the conditions used for the GITT experiments, more lithium was extracted from the cathode materials than during the constant current cycling experiments between 4.3-2.0V described earlier. Compositions corresponding to the high states-of-charge where lithium diffusion slows significantly are not normally achieved in the galvanostatic experiments, particularly for cells containing electrode materials with high levels of Al-substitution. In fact, Al-substitution appears to limit composition changes to a range with the highest average rates of lithium diffusion, during cycling to 4.3V.

*$Li[Ni_{0.4}Co_{0.15}Fe_{0.05}Mn_{0.4}]O_2$*

Under the synthesis conditions employed here, iron substitution appears to be limited to about y=0.05 in $Li[Ni_{0.4}Co_{0.2-y}Fe_y]O_2$. Unlike aluminum, iron is electrochemically active in the same potential window as the $Ni^{2+}/Ni^{4+}$ redox couple so that the substitution of iron for cobalt has a negligible impact on the theoretical capacity for the composition $Li[Ni_{0.4}Co_{0.15}Fe_{0.05}Mn_{0.4}]O_2$ (279 mAh/g).

The XRD patterns of $Li[Ni_{0.4}Co_{0.15}Fe_{0.05}Mn_{0.4}]O_2$ and $Li[Ni_{0.4}Co_{0.2}Mn_{0.4}]O_2$ are presented in Figure 10. The shift in the 003 reflection to lower 2Θ indicates an expansion in the *c* axis upon the incorporation of iron and is a positive indication of solid solution formation. Table I contains the results of the Rietveld refinement of the combined XRD and neutron data. Both the *a* and *c* unit cell parameters increase slightly (0.2%) upon iron substitution. The increased distance between transition metal ions can be explained by the larger ionic radius of high spin $Fe^{3+}$ in six-fold coordination (0.645

Å) relative to low-spin $Co^{3+}$(0.545Å).[14] The lithium slab dimension is unchanged, and the anti-site defect concentration is slightly increased relative to the parent compound.

The pressed pellet conductivity of $LiNi_{0.4}Co_{0.15}Fe_{0.05}Mn_{0.4}O_2$ is compared to that of $LiNi_{0.4}Co_{0.2}Mn_{0.4}O_2$ in Figure 11. The electronic conductivity of the latter is $1.1x10^{-5}$ S/cm at 75° C and for the former it decreases to $2.7x10^{-8}$ S/cm. The activation energy rises to 0.660 eV, indicating increased difficulty in moving the charge-carrying defects. This result is intriguing; iron has *d*-states available near the Fermi energy and iron substituted materials have been calculated to have smaller band gaps than unsubstituted materials. This would indicate that the thermally driven formation of charged defects, either electrons or holes, should be more favorable in the substituted system.[27] The observed trends may relate more to a disruption in the cobalt bonding network than the presence of the iron substituent.

$Li[Ni_{0.4}Co_{0.15}Fe_{0.05}Mn_{0.4}]O_2$ exhibits a reduced capacity compared to $Li[Ni_{0.4}Co_{0.2}Mn_{0.4}]O_2$ when cycled in lithium cells between 2.0 and 4.3V or 4.7V at 0.1 $mA/cm^2$, and fading is more rapid (Figure 12). The first cycle irreversible capacity is relatively insensitive to the charge cutoff limit (16.8% for 4.3V and 19.6% for 4.7V) unlike that of cells containing $Li[Ni_{0.4}Co_{0.2-y}Al_yMn_{0.4}]O_2$ cathodes. This suggests a different source for these losses. In other iron-containing compounds, a sharp decrease in lithium mobility near the end of discharge has been observed.[50] The performance of $Li[Ni_{0.4}Co_{0.15}Fe_{0.05}Mn_{0.4}]O_2$ is also markedly inferior to that of $Li[Ni_{0.4}Co_{0.15}Al_{0.05}Mn_{0.4}]O_2$ (compare Figure 5), although the average peak potential is shifted to nearly the same degree (not shown). The rate behavior of $Li[Ni_{0.4}Co_{0.15}Fe_{0.05}Mn_{0.4}]O_2$ cathodes is similar to that of $Li[Ni_{0.4}Co_{0.2}Mn_{0.4}]O_2$ (Figure

13) and is consistent with the structural data, specifically the nearly identical lithium slab dimensions. It is interesting to note that the amount of anti-site mixing in $Li[Ni_{0.4}Co_{0.15}Fe_{0.05}Mn_{0.4}]O_2$ and $Li[Ni_{0.4}Co_{0.15}Al_{0.05}Mn_{0.4}]O_2$ is comparable, but *I(LiO₂)* is still larger in the latter.

**Conclusions**

Several layered oxide positive electrode materials with the formula $Li[Ni_{0.4}Co_{0.2-y}M_yMn_{0.4}]O_2$ (M=Al, Fe) have been synthesized successfully. Aluminum is found to be soluble over the entire composition range ($0 \leq y \leq 0.2$) with no second phase impurities observed. Refinement of structural data indicates that the anti-site defect concentration is slightly elevated upon substitution. However, the lithium slab dimension also becomes larger due to structural effects associated with the partial replacement of Co with a smaller ion. These structural effects have a beneficial effect on the rate performance in lithium cells. The performance of $Li[Ni_{0.4}Co_{0.15}Al_{0.05}Mn_{0.4}]O_2$ is particularly notable, as the aluminum substitution has very little effect on capacity at low rates but utilization is more than doubled at higher current densities. Aluminum-containing materials also exhibit better cycling stability than the parent compound. The formation of single-phase iron containing compounds was limited to y=0.05. There is a slight increase in the anti-site defect concentration and no change in the lithium slab dimension upon substitution with iron. Cells containing $Li[Ni_{0.4}Co_{0.15}Fe_{0.05}Mn_{0.4}]O_2$ cycled to 4.3 V showed reduced capacity compared to $Li[Ni_{0.4}Co_{0.2}Mn_{0.4}]O_2$ even though iron should be electroactive in the operating voltage range, and there is no rate enhancement effect. The results on $Li[Ni_{0.4}Co_{0.15}Fe_{0.05}Mn_{0.4}]O_2$ and $Li[Ni_{0.4}Co_{0.2-}$

$_yAl_yMn_{0.4}]O_2$ compounds show that substituent effects in the mixed transition metal oxides are complex. It may not be necessary to select metals as full or partial replacements for Co that are electroactive or that cause a reduction in anti-site mixing if the lithium slab spacing can be made greater by other means, as is demonstrated with Al substitution.

**Acknowledgments**

This work was supported by the Assistant Secretary for Energy Efficiency and Renewable Energy, Office of Vehicle Technologies of the U.S. Department of Energy under Contract No. DE-AC02-05CH11231. Neutron patterns were obtained at the Lujan Center at the Los Alamos Neutron Science Center, funded by the DOE Office of Basic Energy Sciences, and Los Alamos National Laboratory, funded by the Department of Energy under contract W-7405-ENG-36. The authors would also like to thank Aaron Kueck for TEM images of the active materials.

**References**

1. T. Nagaura, *Progr. in Batt. & Batt. Mat.*, **10**, 218 (1991).

2. M. S. Whittingham, *Chem. Rev.*, **104**, 4271 (2004).

3. N. Yabuuchi, Y. Koyama, N. Nakayama, and T. Ohzuku, *J. Electrochem. Soc.*, **152**, A1434 (2005).

4. T. Ohzuku and Y. Makimura, *Chem. Lett.,* **7**, 642 (2001).

5. M. Ma, N. Chernova, B. H. Toby, P. Y. Zavalij, and M. S. Whittingham, *J. Power Sources*, **165**, 517 (2007).

6. S. Yang, Y. Song, K. Ngala, P.Y. Zavalij, and M. S. Whittingham, *J. Power Sources,* **119-121**, 239 (2003).

7 . A. Van der Ven, G. Ceder, M. Asta, and P.D. Tepesch, *Phys. Rev. B*, **64**, 184307 (2001).

8 . A. Van der Ven and G. Ceder, *J. Power Sources,* **97-98**, 529 (2001).

9. K. Kang and G. Ceder, *Phys. Rev. B*, **74**, 094105-7 (2006).

10. A. Rougier, P. Gravereau, and C. Delmas, *J. Electrochem. Soc.*, **143**, 1168 **(**1996).

11. A. Rougier, I. Saadoune, P. Gravereau, P. Willmann and C. Delmas, *Sol. St. Ionics,* **90**, 83 **(**1996).

12. I. Saadoune, and C. Delmas, *J. Mater. Chem.*, **6**, 193 (1996).

13. J. K. Ngala, N.A. Chernova, M. Ma, M. Mamak, P.Y. Zavalij and M.S. Whittingham, *J. Mater. Chem.*, **14**, 214 (2004).

14. R. Shannon, *Acta Crystallogr. A*, **32**, 751 (1976).

15. K. S. Kang, Y.S. Meng, J. Bréger, C. P. Grey, and G. Ceder, *Science*, **311**, 977 **(**2006).

16. E.J.Wu, P.D. Tepesch, and G. Ceder, *Phil. Mag. B-Physics of Condensed Matter Statistical Mechanics, Electronic, Optical, and Magnetic Properties,* **77**, 1039 (1998).

17. J. Wilcox, S. Patoux, and M. Doeff, *J. Electrochem. Soc*. **156**, A192 (2009).

18. S. Albrecht, J. Kümpers, M. Kruft, S. Malcus, C. Vogler, M. Wahl, and M. Wohlfahrt-Mehrens, *J. Power Sources*, **119-121**, 178 (2003).

19. F. Zhou, X. Zhao, Z. Lu, J. Jiang, and J.R. Dahn, *Electrochem. Commun.*, **10**, 1168 (2008).

20. F. Zhou, X. Zhao, Z. Lu, J. Jiang and J. R. Dahn, *Electrochem. and Solid St. Lett.,* **11**, A155 (2008).

21. T.A. Hewston and B.L. Chamberland, *J. Phys. and Chem. Solids.*, **48**, 97 (1987).

22. M. Wang, and A. Navrotsky, *J. Sol. St. Chem.*, **178**, 1230 (2005).

23. D. E. Cox, G. Shirane, P.A. Flinn, S. L. Ruby, and W. J. Takei, *Phys. Rev.,* **132**, 1547 (1963).

24. J. C. Anderson and M. Schieber, *J. Phys. and Chem. Sol.,* **25**, 961 (1964).

25. J. Morales, J. and J. Santos-Pena, *Electrochem. Commun.*, **9**, 2116 (2007).

26. K. Ado, M. Tabuchi, H. Kobayashi, H. Kageyama, O. Nakamura, Y. Inaba, R. Kanno, M. Tagaki, and Y. Takeda, *J. Electrochem. Soc.*, **144**, L177 (1997).

27. Y.S. Meng, Y. W. Wu, B. J. Hwang, Y. Li, and G. Ceder, *J. Electrochem. Soc.*, **151**, A1134 (2004).

28. J. N. Reimers, E. Rossen, C. D. Jones, and J. R. Dahn, *Sol. St. Ionics*, **61**, 335 **(**1993).

29. J.R.Mueller-Neuhaus, R.A. Dunlap, and J.R. Dahn, *J. Electrochem. Soc.*, **147**, 3598 (2000).

30. C. Delmas, M. Ménétrier, L. Croguennec, I. Saadoune, A. Rougier, C. Pouillerie, G. Prado, M. Grüne, and L. Fournès, *Electrochim. Acta*, **45**, 243 (1999).

31. J. Wilcox and M. Doeff, *ECS Transactions*, **11**, 27 (2008).

32. A.C. Larson, and R.B. Von Dreele, *Los Alamos National Laboratory Report LAUR*, **86**, 748 (2000).

33. B. H. Toby, *J. Appl. Cryst.,* **34**, 210 (2001).

34 . S. Chung and Y. -M. Chiang, *Electrochem. and Solid State Lett.,* **6,** A278 (2003).

35. J. Molenda, A. Stoklosa, and T. Bak, *Sol. State Ionics*, **36,** 53 (1989).

36. S.-K. Hu, T.-C. Chou, B.-J. Hwang, and G. Ceder *J. Power Sources*, **160**, 1287 (2006).

37. K. Persson and M. Kocher, unpublished results.

38. A. Deb, U. Bergmann, S.P. Cramer and E.J. Cairns, *J. Electrochem. Soc.*, **154**, A534 (2007).

39. Y. W. Tsai, B. J. Hwang, G. Ceder, H. S. Sheu, D. G. Liu, and J. F. Lee, *Chem. Mater.,* **17**, 3191 (2005).

40. Y. Koyama, I. Tanaka, H. Adachi, Y. Makimura, T. Ohzuku, *J. Power Sources,* **119**, 644 (2003).

41. B. J. Hwang, Y. W. Tsai, D. Carlier, and G. Ceder, *Chem. Mater.*, **15**, 3676 (2003).

42. J. Choi, and A. Manthiram, *J. . Electrochem. Soc.*, **152**, A1714 (2005).

43. K. M. Shaju, G.V. Subba Rao, and B.V.R. Chowdari, *Electrochim. Acta*, **48**, 145 (2002).

44. S.-K. Hu, T.-C. Chou, B.-J. Hwang, and G. Ceder *J. Power Sources*, **160**, 1287 (2006).

45. J. Choi, and A. Manthiram, *Electrochem. and Sol..State Lett.*, **8**, C102 (2005).

46. C. J. Wen, B.A. Boukamp, and R.A. Huggins, *J. Electrochem. Soc.*, **126**, 2258 (1979).

47. J. S. Hong and J.R. Selman, *J. Electrochem. Soc.*, **147**, 3190 (2000).

48. K.M.Shaju, G.V.S. Rao, and B.V.R. Chowdari, *J. Electrochem. Soc.,* **150** A1 (2003).

49. A. Van der Ven, J. C. Thomas, Q. Xu, B. Swoboda, and D. Morgan, *Phys. Rev. B,* **78**, 104306 (2008).

50. J. R. Mueller-Neuhaus, R.A. Dunlap, and J.R. Dahn, *J. Electrochem. Soc.,* **147**, 3598 (2000).

## Tables

**Table 1.** Crystal structure parameters for $Li[Ni_{0.4}Co_{0.2-y}M_yMn_{0.4}]O_2$ compounds from combined X-ray and neutron diffraction Rietveld refinements.[a]

| y/M | Unit Cell Parameters | | $z_{Ox}$ | Unit Cell Volume (Å$^3$) | $Ni_{3a}$ | $I$ ($LiO_2$) (Å) | $R_{wp}$ (%) |
|---|---|---|---|---|---|---|---|
| | a (Å) | c (Å) | | | | | |
| 0 | 2.87238(2) | 14.2688(2) | 0.24165(3) | 101.954(2) | 0.066(1) | 2.616(1) | 4.26 |
| 0.05/Al | 2.87242(2) | 14.2729(2) | 0.24153(3) | 101.987(2) | 0.073(1) | 2.621(1) | 4.46 |
| 0.10/Al | 2.87169(3) | 14.2854(2) | 0.24168(3) | 102.024(2) | 0.075(1) | 2.619(1) | 4.92 |
| 0.15/Al | 2.86970(3) | 14.2896(3) | 0.24159(3) | 101.913(2) | 0.074(1) | 2.622(1) | 4.98 |
| 0.20/Al | 2.86900(2) | 14.2993(2) | 0.24159(3) | 101.932(2) | 0.074(1) | 2.624(1) | 5.35 |
| 0.05/Fe | 2.88027(4) | 14.2930(4) | 0.24180(1) | 102.689(2) | 0.072(1) | 2.617(1) | 4.53 |

a) Standard uncertainties from the structural refinements are shown in parentheses.

**Table 2.** Activation energies for electron transport as a function of composition in $Li[Ni_{0.4}Co_{0.2-y}Al_yMn_{0.4}]O_2$ ($0 \leq y \leq 0.2$) compounds.

| y | $E_a$ (eV) |
|---|---|
| 0 | 0.346 |
| 0.05 | 0.361 |
| 0.1 | 0.639 |
| 0.15 | 0.708 |
| 0.2 | 0.752 |

**Figure Captions**

1. XRD powder patterns of $Li[Ni_{0.4}Co_{0.2-y}Al_yMn_{0.4}]O_2$ compounds.

2. Transmission electron micrographs of a) $Li[Ni_{0.4}Co_{0.2}Mn_{0.4}]O_2$, b) $Li[Ni_{0.4}Al_{0.2}Mn_{0.4}]O_2$ and c) scanning electron micrograph of $Li[Ni_{0.4}Co_{0.2}Mn_{0.4}]O_2$ powder after sintering in air at 800° C. This morphology is typical of all the powders used in the study.

3. Rietveld refinement results from (a) Bank 1 (40°), (b) Bank 2 (90°), (c) Bank 3 (119°), (c) Bank 4 (148°), and (e) XRD for the composition $Li[Ni_{0.4}Co_{0.2}Mn_{0.4}]O_2$. Black dots and red lines represent the experimental data and calculated fit, respectively. Allowed Bragg reflections are marked as black bars and the difference between the experimental data and calculated fit is noted in blue. The structural parameters from the refinement are given in Table 1.

4. Conductivities of $Li[Ni_{0.4}Co_{0.2-y}Al_yMn_{0.4}]O_2$ ($0 \leq y \leq 0.2$) pressed pellets as a function of temperature.

5. Discharge capacities of $Li/Li[Ni_{0.4}Co_{0.2-y}Al_yMn_{0.4}]O_2$ ($0 \leq y \leq 0.2$) cells cycled at a constant charge and discharge current density of 0.1 $mA/cm^2$ between (a) 2.0-4.3 V or (b) 2.0-4.7 V.

6. Differential capacity (dQ/dV) vs. cell potential for $Li/LiNi_{0.4}Co_{0.2-y}Al_yMn_{0.4}O_2$ ($0 \leq y \leq 0.2$) cells charged and discharged between 2.0-4.3 V at 0.1 $mA/cm^2$ (first cycles).

7. First cycles of $Li/Li[Ni_{0.4}Co_{0.2-y}Al_yMn_{0.4}]O_2$ ($0 \leq y \leq 0.2$) cells charged and discharged at 0.1 $mA/cm^2$ between 2.0-4.3V or 2.0-4.7V: a) y=0, b) y=0.05, c) y=0.1, d) y=0.15, and e) y=0.2. A table showing average irreversible capacity losses for each type of cell is included.

8. Capacity as a function of current density for Li/Li[$Ni_{0.4}Co_{0.2-y}Al_yMn_{0.4}$]$O_2$ cells charged at 0.1 mA/$cm^2$ and discharged at 0.1, 0.5, 1, 2, and 3 mA/$cm^2$ between 2.0-4.3 V: a)y=0, b) y=0.05, c) y=0.1, d) y=0.15, and e) y=0.2. A modified Peukert plot summarizing results as a function of y in $LiNi_{0.4}Co_{0.2-y}Al_yMn_{0.4}O_2$ is shown in f).

9. Relative diffusion coefficients as a function of state-of-charge obtained from GITT experiments on Li/Li[$Ni_{0.4}Co_{0.2-y}Al_yMn_{0.4}$]$O_2$, ($0 \leq y \leq 0.2$) cells. Data was taken between 2.0 and 4.4V using current steps of 0.135 mA lasting 40.5 minutes with 4 hour rests between steps.

10. XRD powder patterns of Li[$Ni_{0.4}Co_{0.2}Mn_{0.4}$]$O_2$ (bottom) and Li[$Ni_{0.15}Co_{0.15}Fe_{0.05}Mn_{0.4}$]$O_2$ (top).

11. Conductivities of Li[$Ni_{0.4}Co_{0.2}Mn_{0.4}$]$O_2$ and Li[$Ni_{0.15}Co_{0.15}Fe_{0.05}Mn_{0.4}$]$O_2$ pressed pellets as a function of temperature.

12. Discharge capacities of Li/Li[$Ni_{0.4}Co_{0.2}Mn_{0.4}$]$O_2$ and Li/ Li[$Ni_{0.15}Co_{0.15}Fe_{0.05}Mn_{0.4}$]$O_2$ cells cycled at a constant charge and discharge current density of 0.1 mA/$cm^2$ between (a) 2.0-4.3 V or (b) 2.0-4.7 V.

13. Rate capabilities of Li/Li[$Ni_{0.4}Co_{0.2}Mn_{0.4}$]$O_2$ and Li/ Li[$Ni_{0.15}Co_{0.15}Fe_{0.05}Mn_{0.4}$]$O_2$ cells charged and discharged between 2.0-4.3 V.

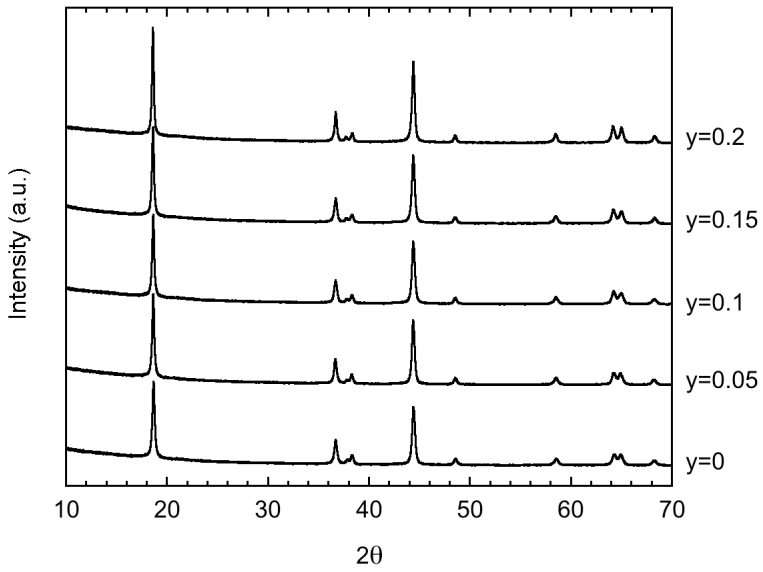


**Figure 1**

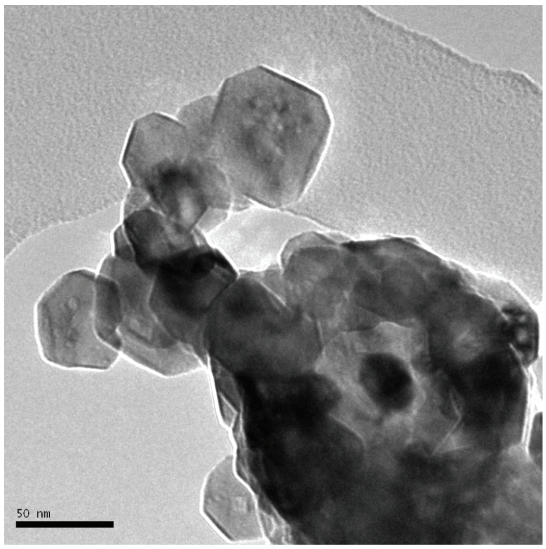


(a)

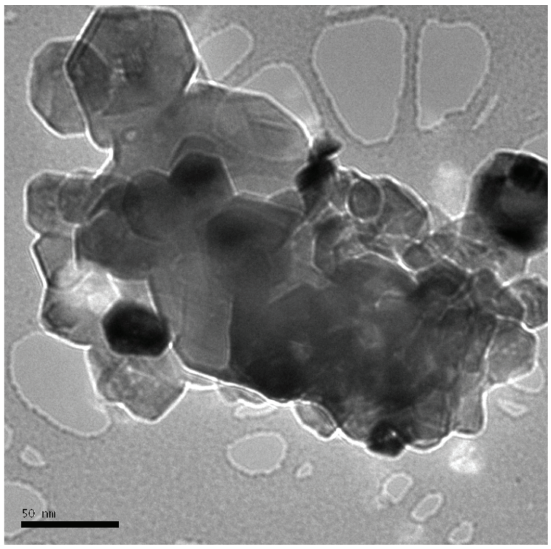


(b)

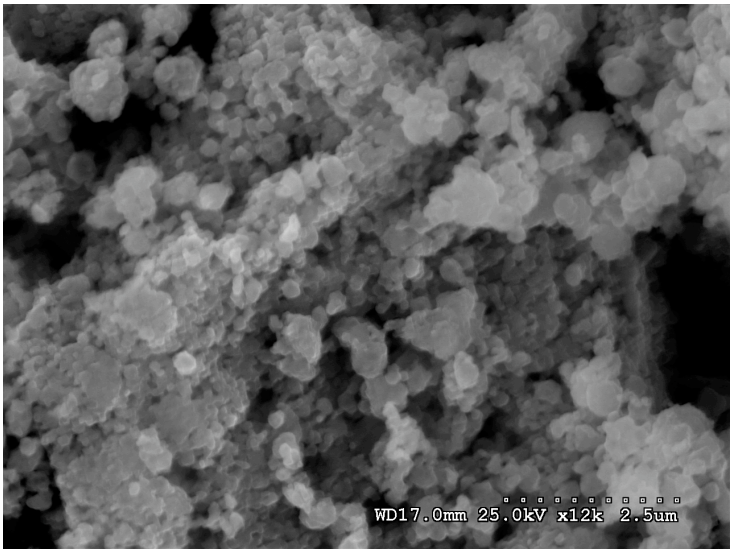


(c)

**Figure 2**

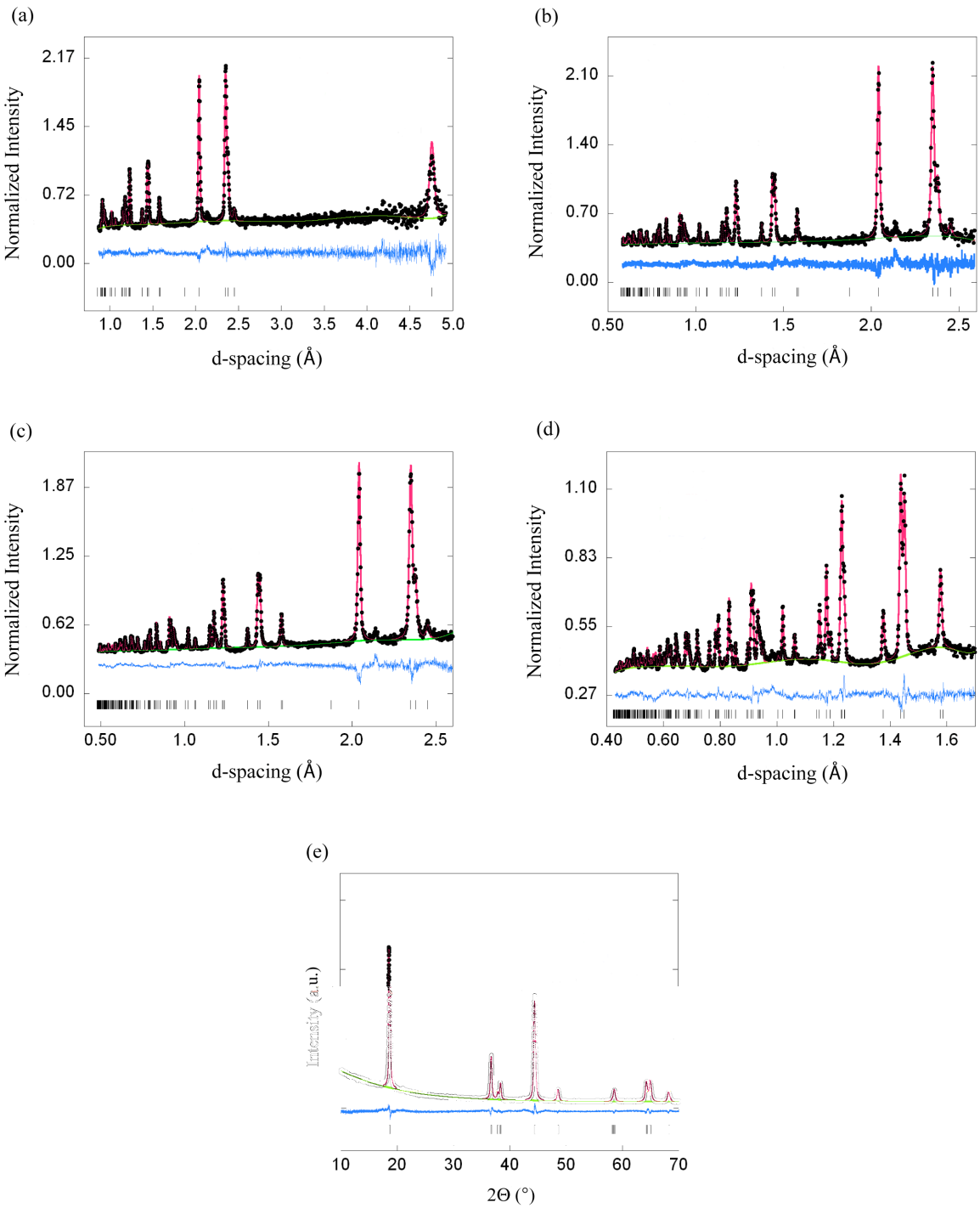
(a)
Normalized Intensity
2.17
1.45
0.72
0.00
1.0 1.5 2.0 2.5 3.0 3.5 4.0 4.5 5.0
d-spacing (Å)
(b)
Normalized Intensity
2.10
1.40
0.70
0.00
0.50 1.0 1.5 2.0 2.5
d-spacing (Å)
(c)
Normalized Intensity
1.87
1.25
0.62
0.00
0.50 1.0 1.5 2.0 2.5
d-spacing (Å)
(d)
Normalized Intensity
1.10
0.83
0.55
0.27
0.40 0.60 0.80 1.0 1.2 1.4 1.6
d-spacing (Å)
(e)
Intensity (a.u.)
10 20 30 40 50 60 70
2Θ (°)

**Figure 3**

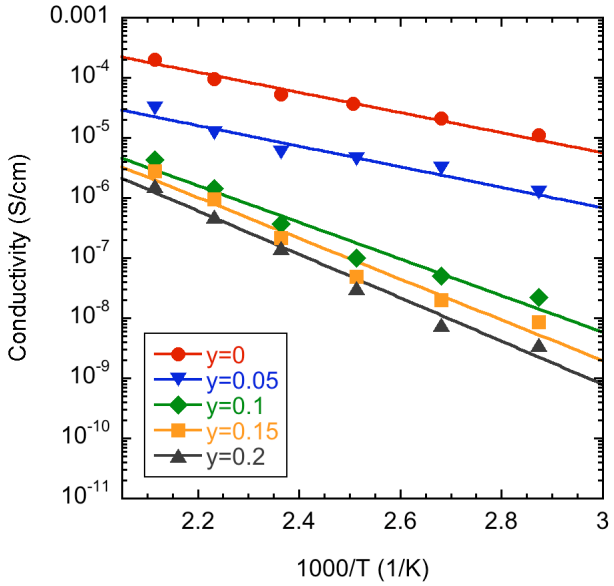
0.001
10-4
10-5
10-6
10-7
10-8
10-9
10-10
10-11
Conductivity (S/cm)
2.2
2.4
2.6
2.8
3
1000/T (1/K)
y=0
y=0.05
y=0.1
y=0.15
y=0.2

**Figure 4**

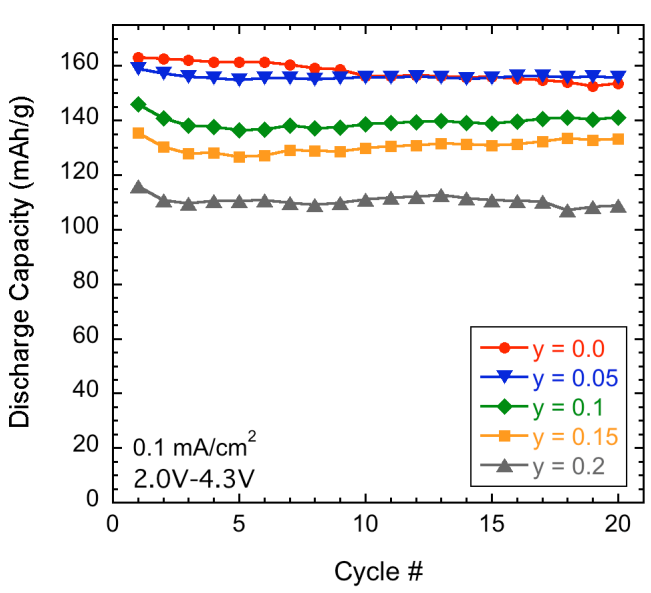
Discharge Capacity (mAh/g)
Cycle #
0.1 mA/cm2
2.0V-4.3V
y = 0.0
y = 0.05
y = 0.1
y = 0.15
y = 0.2

(a)

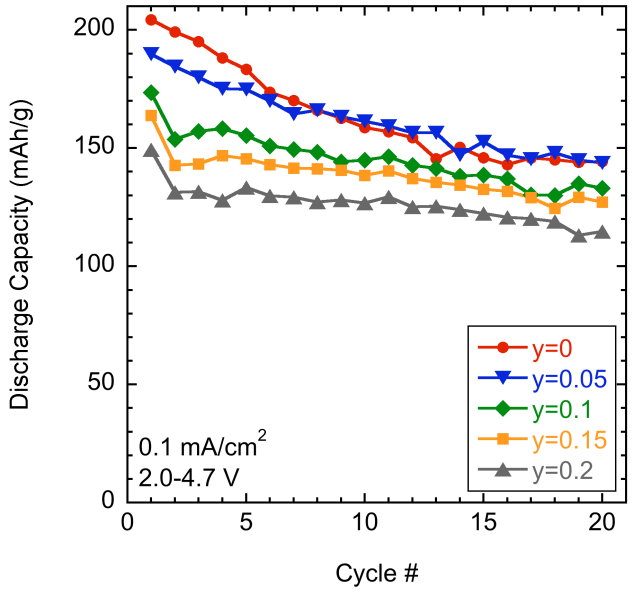
Discharge Capacity (mAh/g)
Cycle #
0.1 mA/cm2
2.0-4.7 V
y=0
y=0.05
y=0.1
y=0.15
y=0.2

(b)

**Figure 5**

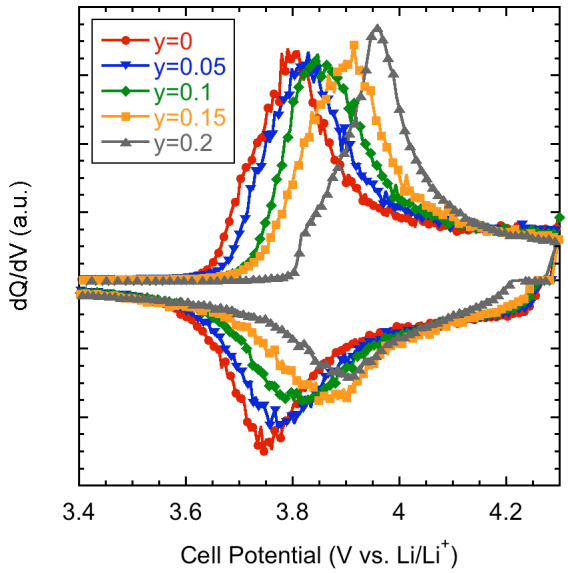
y=0
y=0.05
y=0.1
y=0.15
y=0.2
dQ/dV (a.u.)
3.4
3.6
3.8
4
4.2
Cell Potential (V vs. Li/Li+)

**Figure 6**

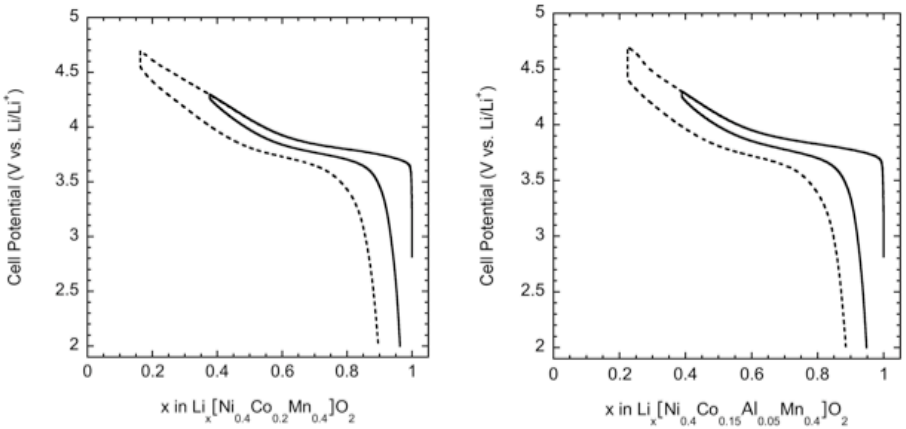


(a)




(b)

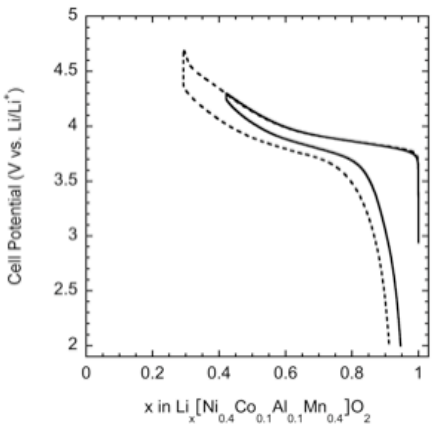


(c)

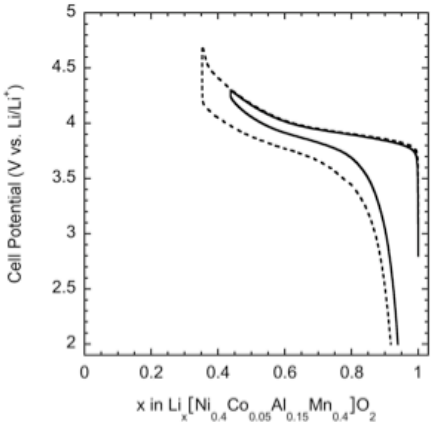


(d)

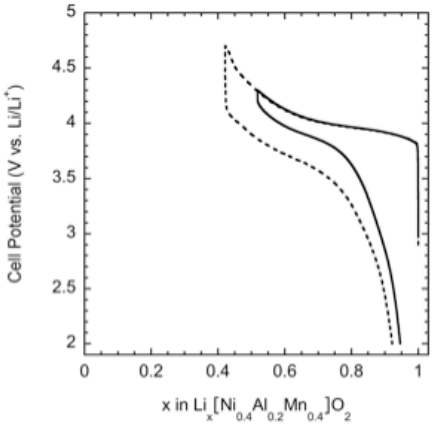


(e)

| y | Irrev. Cap. Loss (%) | |
|---|---|---|
| | to 4.3V | to 4.7V |
| 0 | 6.10±0.47 | 14.32±0.2 |
| 0.05 | 9.18±1.6 | 17.27±0.1 |
| 0.1 | 13.24±2.2 | 14.83±1.0 |
| 0.15 | 14.20±2.6 | 15.17±0.9 |
| 0.2 | 14.14±4.1 | 20.86±5.2 |

**Figure 7**

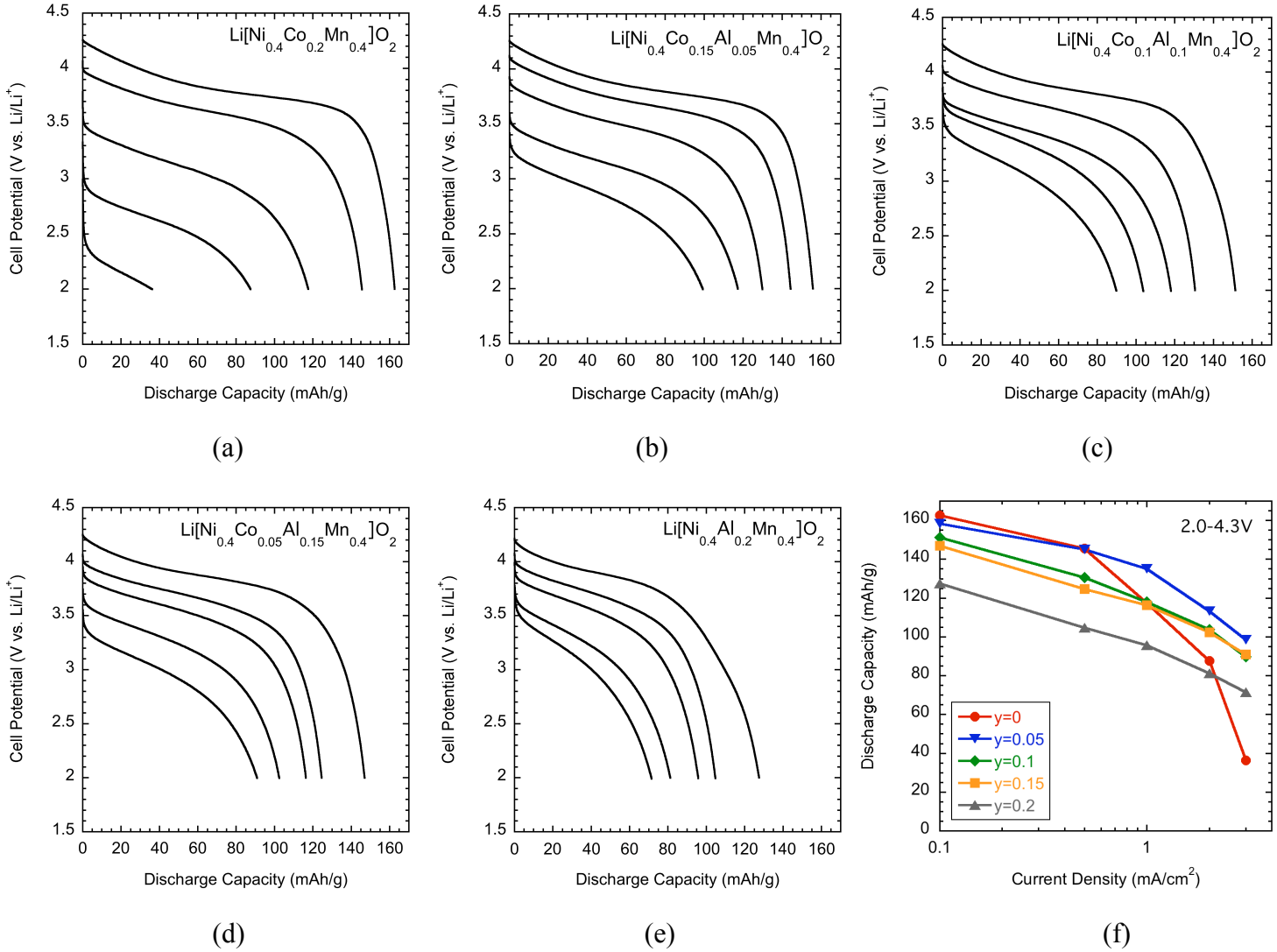
Li[Ni0.4Co0.2Mn0.4]O2
Li[Ni0.4Co0.15Al0.05Mn0.4]O2
Li[Ni0.4Co0.1Al0.1Mn0.4]O2
Li[Ni0.4Co0.05Al0.15Mn0.4]O2
Li[Ni0.4Al0.2Mn0.4]O2
Cell Potential (V vs. Li/Li+)
Discharge Capacity (mAh/g)
Discharge Capacity (mAh/g)
Current Density (mA/cm2)
2.0-4.3V
y=0
y=0.05
y=0.1
y=0.15
y=0.2
(a)
(b)
(c)
(d)
(e)
(f)

**Figure 8**

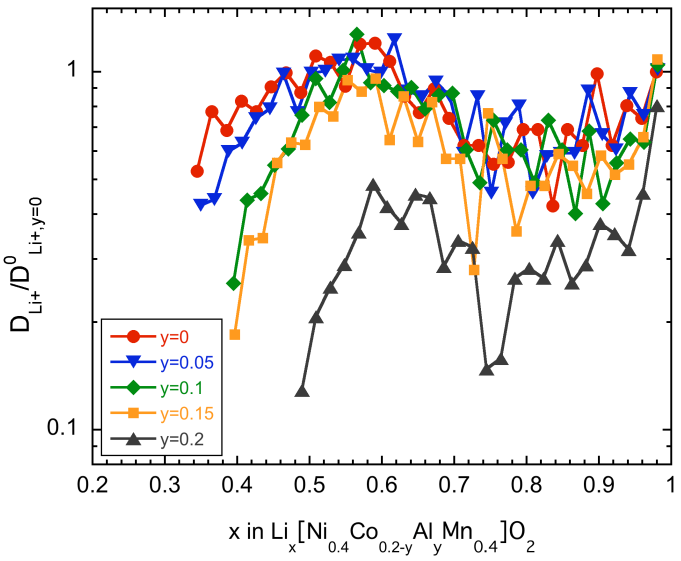
1
0.1
$D_{Li+}/D^0_{Li+,y=0}$
y=0
y=0.05
y=0.1
y=0.15
y=0.2
0.2
0.3
0.4
0.5
0.6
0.7
0.8
0.9
1
x in $Li_x[Ni_{0.4}Co_{0.2-y}Al_yMn_{0.4}]O_2$

**Figure 9**

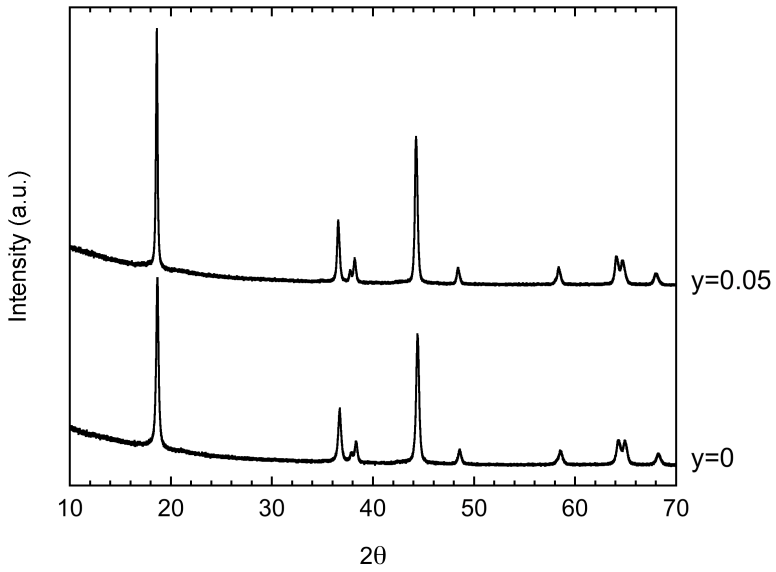


**Figure 10**

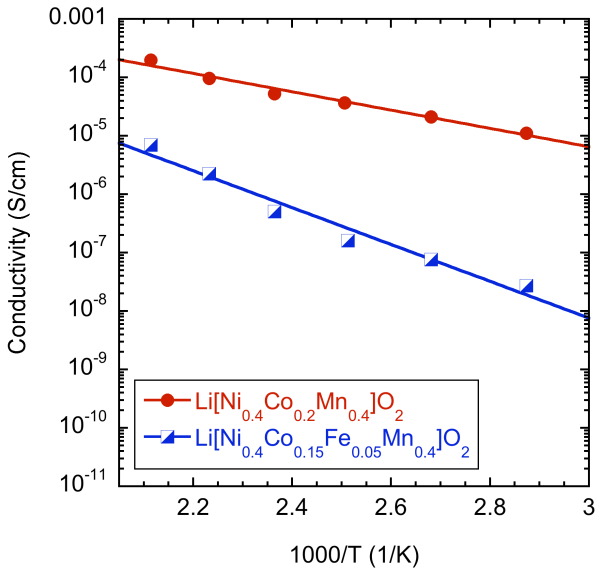
0.001
10-4
10-5
10-6
10-7
10-8
10-9
10-10
10-11
Conductivity (S/cm)
2.2
2.4
2.6
2.8
3
1000/T (1/K)
Li[Ni0.4Co0.2Mn0.4]O2
Li[Ni0.4Co0.15Fe0.05Mn0.4]O2

**Figure 11**

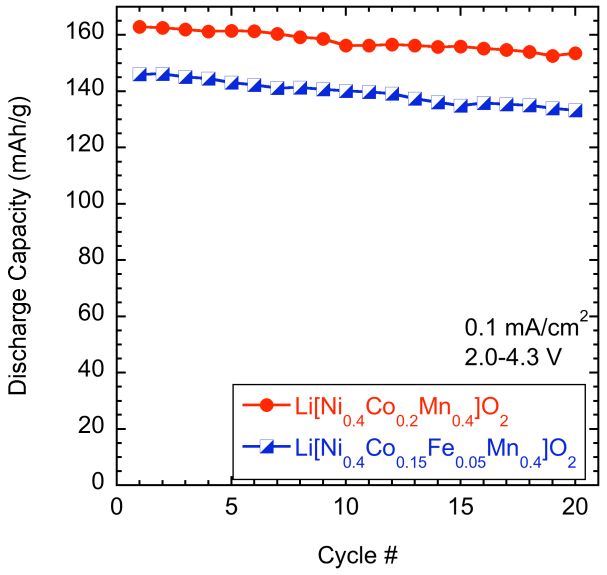
Discharge Capacity (mAh/g)
Cycle #
0.1 mA/cm2
2.0-4.3 V
Li[Ni0.4Co0.2Mn0.4]O2
Li[Ni0.4Co0.15Fe0.05Mn0.4]O2

(a)

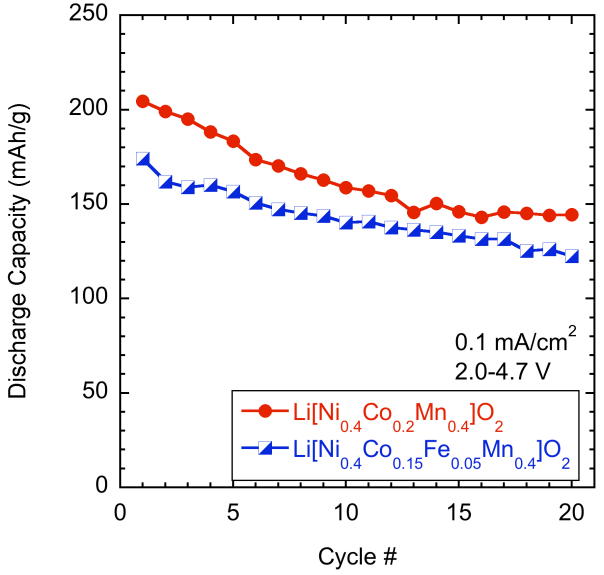
Discharge Capacity (mAh/g)
Cycle #
0.1 mA/cm2
2.0-4.7 V
Li[Ni0.4Co0.2Mn0.4]O2
Li[Ni0.4Co0.15Fe0.05Mn0.4]O2

(b)

**Figure 12**

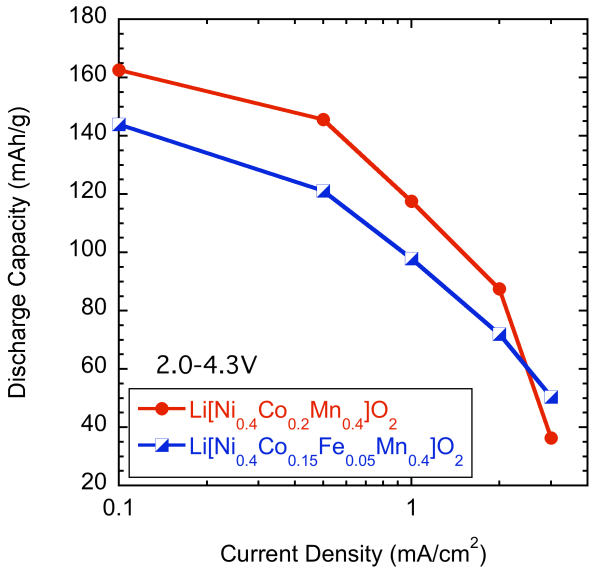
180
160
140
120
100
80
60
40
20
0.1
1
Discharge Capacity (mAh/g)
Current Density (mA/cm2)
2.0-4.3V
Li[Ni0.4Co0.2Mn0.4]O2
Li[Ni0.4Co0.15Fe0.05Mn0.4]O2

**Figure 13**